

Turbo-ICL: In-Context Learning-Based Turbo Equalization

Zihang Song, Matteo Zecchin, Bipin Rajendran and Osvaldo Simeone

Abstract—This paper introduces a novel in-context learning (ICL) framework, inspired by large language models (LLMs), for soft-input soft-output channel equalization in coded multiple-input multiple-output (MIMO) systems. The proposed approach learns to infer posterior symbol distributions directly from a prompt of pilot signals and decoder feedback. A key innovation is the use of prompt augmentation to incorporate extrinsic information from the decoder output as additional context, enabling the ICL model to refine its symbol estimates iteratively across turbo decoding iterations. Two model variants, based on Transformer and state-space architectures, are developed and evaluated. Extensive simulations demonstrate that, when traditional linear assumptions break down, e.g., in the presence of low-resolution quantization, ICL equalizers consistently outperform conventional model-based baselines, even when the latter are provided with perfect channel state information. Results also highlight the advantage of Transformer-based models under limited training diversity, as well as the efficiency of state-space models in resource-constrained scenarios.

Index Terms—In-context learning, turbo equalization, multiple-input multiple-output (MIMO), sequence models, Transformer, state-space model

I. INTRODUCTION

A. Context and Motivation

Turbo equalization iteratively exchanges soft information between the equalizer and decoder to approach near-optimal decoding performance in coded communication systems [1]. Since its introduction in the 1990s [2], numerous soft-input soft-output equalizers have been developed to implement this concept. Notable examples include linear minimum mean-square error (LMMSE) equalizers with parallel interference cancellation (PIC) [3], [4] and soft-output sphere decoders [5], [6]. In multiple-input multiple-output (MIMO) systems, such equalizers are typically combined with iterative channel estimation techniques like recursive least squares (RLS), allowing the receiver to refine both the channel estimate and data detection across iterations [7].

Despite their success, conventional turbo equalizers rely heavily on accurate channel modeling and often assume Gaussian noise and a linear front end at the receiver [3]. These assumptions become limiting under severe hardware impairments or limited-resolution receiver front ends [8].

The authors are with the Centre for Intelligent Information Processing Systems (CIIPS), Department of Engineering, King’s College London, London WC2R 2LS, U.K. (e-mail: {zihang.song, matteo.i.zecchin, bipin.rajendran, osvaldo.simeone}@kcl.ac.uk).

This work is supported in part by the European Union’s Horizon Europe project CENTRIC (101096379), the EPSRC project (EP/X011852/1), and the Open Fellowships of the EPSRC (EP/W024101/1 and EP/X011356/1).

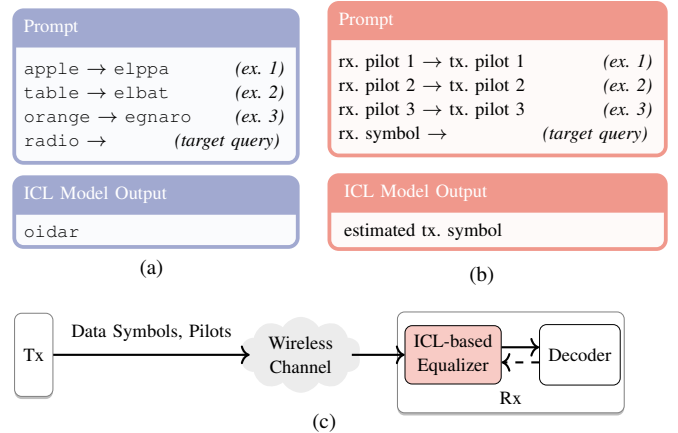


Fig. 1. (a) Example of a prompt and the corresponding output of a large language model (LLM) performing in-context learning (ICL). Given a few input-output examples of a task (e.g., word reversal), the model generalizes the underlying pattern and produces the correct output for a new query. (b)-(c) The same principle can be applied to the task of channel equalization. The ICL-based equalizer is prompted with a set of channel input-output pairs, corresponding to pilots, along with a received data symbol, and it returns the estimated transmitted symbol.

More recently, machine learning techniques have been explored to enhance or replace model-based equalization. For example, deep neural networks have been applied to nonlinear channel equalization in optical fiber systems [9]. While such neural equalizers can mitigate complex distortion effects, e.g., based on recurrent or convolutional architectures, they typically need extensive retraining or fine-tuning for each specific channel and lack the flexibility to generalize across diverse conditions [10]. This motivates the search for more adaptive approaches that can learn on the fly from data, without explicit channel models or per-channel re-training.

In-context learning (ICL), a capability emerged in large language models (LLMs), has become a promising neural paradigm for adaptive communication receivers. In an ICL-based equalizer, a sequence model – such as a Transformer or *state-space model* (SSM) – is provided with a prompt consisting of known transmitted–received pilot symbol pairs, enabling it to invert the underlying channel mapping directly from those examples (see Fig. 1). This essentially performs on-the-fly adaptation to the current channel conditions without needing explicit channel state information (CSI) [11]–[14].

Early demonstrations of ICL for MIMO detection have shown superior performance compared to traditional model-based methods, particularly in non-linear or highly quantized scenarios and when only a short pilot is available [11], [12].

This indicates that ICL-based equalizers can directly learn to compensate for complex channel impairments from pilot data, offering a new CSI-free approach to signal detection.

However, integrating ICL into turbo equalization remains an open challenge. Existing ICL equalizers [11]–[14] operate in a single-pass fashion, producing one-shot decisions for data symbols without accounting for any decoder feedback. Furthermore, many of these methods output only hard decisions, i.e., point estimates of symbols, rather than soft probability distributions [15]. As a result, they cannot participate in the iterative exchange of soft information that turbo decoding requires. In essence, current ICL-based receivers are incompatible with turbo processing, since they neither generate the a posteriori probabilities needed to compute *log-likelihood ratios* (LLRs) nor update estimates based on decoder-generated priors.

This gap motivates our work: to develop an ICL-based equalization approach that fully embraces the turbo principle, delivering soft outputs and refining its detection with decoder feedback. By addressing this need, we aim to unlock the benefits of ICL for coded communication systems, where robust iterative equalization is critical for reliability under challenging channel conditions.

B. Related Work

Turbo Equalization: The concept of turbo equalization, as introduced by [2], combined convolutional decoding with iterative detection to correct inter-symbol interference. A comprehensive overview of turbo equalization is provided by [7], covering early developments in soft-output detection. Subsequent research produced a variety of soft equalizers that improved performance and complexity. For instance, the LMMSE-PIC detector by [3], [4] achieves hardware-friendly soft-output MIMO detection. Soft sphere decoding methods were shown by [5], [6] to approach MIMO capacity at the cost of complexity. Probabilistic data association-based schemes were explored as an alternative iterative detection approach leveraging probabilistic inference. To handle time-varying channels, adaptive turbo equalizers with online channel estimation (e.g., via RLS) have been proposed [16].

Turbo equalization has also been extended beyond ideal linear models. Researchers have investigated receivers for one-bit and low-resolution ADC systems [17], using Busgang decomposition and other techniques [18], [19] to mitigate quantization nonlinearity. These studies collectively established the feasibility of turbo equalizers in many scenarios, but their dependence on accurate channel models and estimators remains a fundamental limitation [7].

Deep Learning-based Equalizers: In the last decade, deep learning has been applied to wireless receivers to relax modeling assumptions. Several works have demonstrated neural network equalizers that learn to inverse the channel distortion from data, often using supervised training. Reference [9] introduced a neural turbo equalization approach for optical communications, where a deep neural network compensates fiber nonlinearity in coordination with soft LDPC decoding. In wireless MIMO systems, a variety of model-driven deep learn-

ing detectors – e.g., employing unfolded iterative algorithms or graph neural networks – have been reported, generally requiring a training phase per channel scenario [20]–[22].

These neural receivers can outperform linear detectors under complex impairments, but they usually lack on-the-fly adaptability. Without retraining or meta-learning, a network trained on one set of channel conditions often fails to generalize to others [10]. In summary, while deep learning provides strong approximation performance, existing approaches lack the ability to leverage real-time context like pilots and decoder outputs for instantaneous adaptation.

ICL-Based Symbol Detectors: Inspired by the success of large-sequence models in natural language tasks, there is growing interest in applying ICL to symbol detection in wireless communications. Reference [11], [12] showed that Transformers can serve as efficient in-context estimators for wireless channels, learning channel effects from a few example transmissions. The work [13] further demonstrated a Transformer-based ICL equalizer for MIMO fading channels, and the work [23] developed a neuromorphic sequence model for energy-efficient ICL detection. More recently, the reference [15] proposed a decision-feedback ICL scheme for block-fading channels, and [24] extended ICL equalization to cell-free massive MIMO using SSMS.

These efforts confirm that ICL is a viable approach to MIMO symbol detection, often yielding error-rate gains over traditional detectors in difficult conditions. However, as discussed, all existing ICL equalizers operate without considering iterative decoder interactions. In fact, they are typically trained to output hard decisions or uncalibrated logits for uncoded symbols, which cannot support turbo decoding loops. To our knowledge, no prior work has realized a soft-output ICL equalizer that can be integrated with forward error correction decoders in an iterative fashion. This paper builds upon the above literature by filling this gap.

C. Main Contributions

In this paper, we bridge the gap between ICL and turbo equalization by proposing the first ICL-based soft equalization framework suitable for iterative decoding. The main contributions are summarized as follows:

- *Soft ICL Equalizer with Turbo-Compatible Prompt Design:* We develop an ICL-based MIMO equalizer capable of estimating the full *a posteriori* distribution of transmitted symbols, while incorporating decoder feedback into the ICL model’s input. Thanks to a novel prompt augmentation technique, at each turbo iteration the decoder’s soft output is converted into additional prompt examples. These are used by the ICL equalizer to iteratively refine its estimates in the form of symbol-wise posterior probabilities. This design allows the ICL equalizer to participate in a turbo loop, updating its internal representation of the channel and symbols as new decoder information becomes available.
- *Generalization Across Channels and Receiver Architectures:* The proposed framework is CSI-free and trained to generalize across a wide range of channel conditions. Using a single

sequence model pre-trained over diverse MIMO channels, signal-to-noise ratios (SNRs), and quantization levels, the ICL equalizer can adapt to new environments with only a few pilot symbols as context. We demonstrate that the same model successfully handles different channel realizations and hardware setups without retraining, making it practical for dynamically varying networks.

- *Comprehensive Performance Benchmarking:* We provide an extensive performance evaluation against practical and idealized model-based baselines. Simulation results for various modulation orders, receiver front-end resolutions, and coding rates show that the ICL equalizer consistently outperforms traditional RLS-LMMSE-PIC detectors, even when those baselines have perfect CSI knowledge. The ICL approach also exhibits superior robustness in low-SNR and heavily quantized regimes, achieving an order-of-magnitude BER reduction compared to adaptive linear soft equalizers.

The rest of the paper is organized as follows: Sec.II introduces the system model; Sec.III reviews conventional turbo equalization; Sec.IV details the proposed ICL-based soft equalization; Sec.V explains the pre-training strategy; Sec.VI presents numerical results; and Sec.VII concludes the paper.

II. SYSTEM MODEL

A. Coded Spatial Multiplexing Transmission

As shown in Fig. 2, we consider an $N_t \times N_r$ MIMO system with spatial multiplexing and a quantized front end at the receiver, where N_t and N_r are the number of transmit and receive antennas, respectively [25]. Following a standard communication pipeline, the information source generates N_t independent *information bit* sequences, each of length K , which are denoted as $\{\mathbf{a}^{(n)} = [a_1^{(n)}, \dots, a_K^{(n)}]\}_{n=1}^{N_t}$. Each information bit stream is independently encoded using a forward error-correcting (FEC) code, producing N_t *codewords* $\{\mathbf{b}^{(n)} = [b_1^{(n)}, \dots, b_{K'}^{(n)}]\}_{n=1}^{N_t}$, each of length K' . The codewords are then scrambled by an interleaver, resulting in the *interleaved codewords* $\{\mathbf{c}^{(n)} = [c_1^{(n)}, \dots, c_{K'}^{(n)}]\}_{n=1}^{N_t}$. The code rate, defined as the ratio of information bits to the codeword length, is given by K/K' .

The transmitter employs M -QAM modulation with the constellation set $\mathcal{S} = \{s_1, s_2, \dots, s_M\}$, where each symbol represents $q = \log_2(M)$ bits. At the n -th transmit antenna, the interleaved codeword $\mathbf{c}^{(n)}$ is divided into blocks of q bits, each of which is mapped to a constellation symbol, resulting in $T = K'/q$ data symbols $\{x_i^{(n)}\}_{i=1}^T$, with $x_i^{(n)} \in \mathcal{S}$. The data symbols transmitted at the i -th channel use form the i -th symbol vector

$$\mathbf{x}_i = [x_i^{(1)}, x_i^{(2)}, \dots, x_i^{(N_t)}]^\top \in \mathcal{S}^{N_t \times 1}. \quad (1)$$

Stacking all transmitted symbol vectors over T channel uses, the complete transmitted symbol matrix is given by

$$\mathbf{X} = [\mathbf{x}_1, \mathbf{x}_2, \dots, \mathbf{x}_T] \in \mathcal{S}^{N_t \times T}. \quad (2)$$

Before transmitting the data symbols, each transmit antenna sends a pilot sequence consisting of T_P pilot symbols, chosen from the same constellation set \mathcal{S} . At the i -th channel use, the

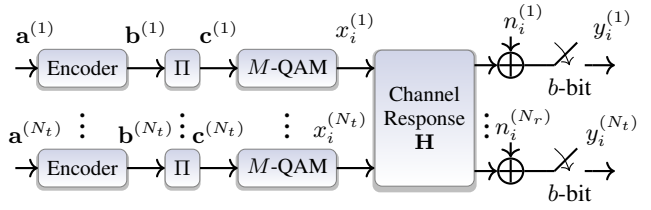


Fig. 2. Block diagrams of coded MIMO transmission with a quantized front end at the receiver.

pilots transmitted from all N_t antennas form the pilot symbol vector

$$\phi_i = [\phi_i^{(1)}, \phi_i^{(2)}, \dots, \phi_i^{(N_t)}]^\top \in \mathcal{S}^{N_t \times 1}. \quad (3)$$

Stacking all transmitted pilot symbol vectors over T_P channel uses, the complete pilot signal matrix is given by

$$\Phi = [\phi_1, \phi_2, \dots, \phi_{T_P}] \in \mathcal{S}^{N_t \times T_P}, \quad (4)$$

where each column represents the pilot symbol vector at a specific channel use. The average transmitted power is normalized as $\mathbb{E}[\|\mathbf{x}_i\|^2] = \mathbb{E}[\|\phi_j\|^2] = N_t$.

We consider a quasi-static fading channel, so that the channel remains constant within a coherence block, consisting of both pilot and data transmissions, which change independently between blocks [26], [27]. Within each coherence block, the received pilot and data symbols before quantization are modeled respectively as

$$\tilde{\mathbf{z}}_j = \mathbf{H}\phi_j + \mathbf{n}_j, \quad j = 1, \dots, T_P, \quad (5a)$$

$$\text{and } \tilde{\mathbf{y}}_i = \mathbf{H}\mathbf{x}_i + \mathbf{n}_i, \quad i = 1, \dots, T, \quad (5b)$$

where $\mathbf{H} \in \mathbb{C}^{N_r \times N_t}$ represents the quasi-static MIMO channel for the given coherence block and $\mathbf{n}_i \sim \mathcal{CN}(\mathbf{0}, \sigma^2 \mathbf{I})$ denotes additive white Gaussian noise with zero mean and variance σ^2 . For simplicity, we assume that the channel coherence block is longer than the frame duration $T_P + T$ so that the transmission of pilots and codeword fits into a single coherence block.

B. Quantized Receiver Front End

At the receiver, the received signals undergo analog-to-digital conversion before processing. Modeling complexity-constrained receivers, we assume that the received signal is processed via a clipping-and-quantization function $Q_B(\cdot)$. Accordingly, they are first clipped within a predefined range $[l_{\min}, l_{\max}]$, and then quantized via a b -bit uniform mid-rise quantizer applied separately to the real and imaginary components of each entry. The resulting quantized signals for pilot and data signals are

$$\mathbf{z}_j = Q_B(\tilde{\mathbf{z}}_j) = Q_B(\mathbf{H}\phi_j + \mathbf{n}_j), \quad j = 1, \dots, T_P, \quad (6a)$$

$$\text{and } \mathbf{y}_i = Q_B(\tilde{\mathbf{y}}_i) = Q_B(\mathbf{H}\mathbf{x}_i + \mathbf{n}_i), \quad i = 1, \dots, T, \quad (6b)$$

respectively, where function $Q_B(\cdot)$ is applied entry-wise.

Stacking all received vectors over the T_P pilots and T data channel uses, the corresponding received pilot and data symbol matrices are denoted as

$$\mathbf{Z} = [\mathbf{z}_1, \mathbf{z}_2, \dots, \mathbf{z}_{T_P}] \in \mathbb{C}^{N_r \times T_P}, \quad (7a)$$

$$\text{and } \mathbf{Y} = [\mathbf{y}_1, \mathbf{y}_2, \dots, \mathbf{y}_T] \in \mathbb{C}^{N_r \times T}, \quad (7b)$$

where each column represents the received quantized signal vector at a given channel use.

The mapping between the transmitted symbols (Φ, \mathbf{X}) and the received signals (\mathbf{Z}, \mathbf{Y}) is parameterized by the channel response \mathbf{H} , noise variance σ^2 , and the quantization parameters $\mathcal{Q} = \{l_{\min}, l_{\max}, B\}$. We define a compact representation for the set of parameters governing the symbol-to-observation mapping as a *task*

$$\tau = \{\mathbf{H}, \sigma^2, \mathcal{Q}\}. \quad (8)$$

For each task τ , the objective of the receiver is to reliably decode the transmitted data \mathbf{X} . As we detail in the next section, this goal is addressed via a turbo equalization architecture that iterates between equalization and decoding [1] (see Fig. 3).

III. TURBO EQUALIZATION

This section first describes the general turbo equalization architecture, then details the conventional implementation based on separate channel estimation and linear equalization [28].

A. Principles of Turbo Equalization

Turbo equalization is an iterative decoding process based on the exchange of information between a *soft equalizer* and a *soft decoder* [7]. Specifically, the soft equalizer and the soft decoder exchange extrinsic log-likelihood ratios (LLRs) of the coded bits.

As illustrated in Fig. 3(a), the soft equalizer estimates the posterior LLR $L(c_k^{(n)}|\mathbf{Y})$ of each coded and interleaved bit $c_k^{(n)}$ based on the received signal \mathbf{Y} and on a prior LLR $L(c_k^{(n)})$. The *channel-extrinsic* LLR, excluding prior information, is then computed as the difference between the posterior and prior LLR,

$$L_e(c_k^{(n)}|\mathbf{Y}) = L(c_k^{(n)}|\mathbf{Y}) - L(c_k^{(n)}). \quad (9)$$

In practice, a clipping operation is commonly applied to avoid numerical instability in the evaluation of the extrinsic LLRs [29]. The extrinsic LLRs (9) are deinterleaved to obtain the extrinsic LLRs of the encoded bits $b_k^{(n)}$, $L_e(b_k^{(n)}|\mathbf{Y})$ which are collected in the vector

$$\mathbf{L}^{(n)} = [L_e(b_1^{(n)}|\mathbf{Y}), \dots, L_e(b_{K'}^{(n)}|\mathbf{Y})]. \quad (10)$$

The decoder takes vectors (10) as input for all streams $n \in \{1, \dots, N_t\}$ to compute the posterior LLRs $L(b_k^{(n)}|\mathbf{L}^{(n)})$ based on the channel code structure [7]. The decoder-extrinsic LLRs are then obtained as the difference

$$L_e(b_k^{(n)}|\mathbf{L}^{(n)}) = L(b_k^{(n)}|\mathbf{L}^{(n)}) - L_e(b_k^{(n)}|\mathbf{Y}). \quad (11)$$

These values are finally re-interleaved to obtain the extrinsic LLRs $L_e(c_k^{(n)}|\mathbf{L}^{(n)})$, which are fed back as the updated prior LLRs $L(c_k^{(n)})$ for the channel equalizer in the next iteration.

Once there is no error in the parity check or a predefined number of iterations has been reached, the final decoded information bits are determined as

$$\hat{a}_k^{(n)} = \begin{cases} 1, & \text{if } L(a_k^{(n)}|\mathbf{L}^{(n)}) > 0, \\ 0, & \text{otherwise,} \end{cases} \quad (12)$$

where $L(a_k^{(n)}|\mathbf{L}^{(n)})$ denotes the estimated posterior LLR of the k -th information bit. In the case of systematic codes, this

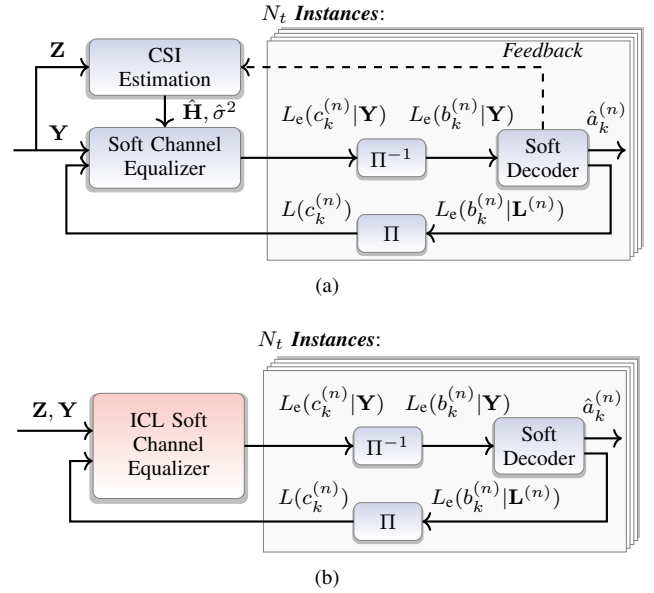


Fig. 3. Block diagrams of turbo equalization (a) with a conventional soft channel equalizer assisted by estimated CSI, and (b) with an ICL soft channel equalizer without explicit CSI estimation.

is obtained directly from the LLRs at the information bit positions in $L(b_k^{(n)}|\mathbf{L}^{(n)})$, whereas for non-systematic codes, this LLR is derived from the decoder's soft output corresponding to the information bits.

B. Conventional Implementation with Channel Estimation and Linear Equalization

We now review the conventional soft equalizer based on the LMMSE criterion [3] and PIC [30]–[32]. To start, the channel estimate $\hat{\mathbf{H}}$ and noise variance $\hat{\sigma}^2$ are obtained from the received pilot symbols \mathbf{Z} , e.g., using the least squares (LS) method

$$\hat{\mathbf{H}} = \mathbf{Z} \Phi^H (\Phi \Phi^H)^{-1}, \quad (13a)$$

$$\text{and } \hat{\sigma}^2 = \frac{1}{N_r T_P} \left\| \mathbf{Z} - \hat{\mathbf{H}} \Phi \right\|_F^2, \quad (13b)$$

where $\|\cdot\|$ denotes Frobenius norm.

At each iteration of the turbo equalization process, given the prior LLR $L(c_k^{(n)})$ obtained from the soft decoder, the prior probability of the transmitted symbol $x_i^{(n)}$ being the m -th constellation point is computed as

$$\Pr(x_i^{(n)} = s_m) = \prod_{\kappa=1}^q \frac{1}{2} \left[1 + (2b_{\kappa,m} - 1) \tanh \left(\frac{L(c_{(i-1)q+\kappa}^{(n)})}{2} \right) \right], \quad (14)$$

where $b_{\kappa,m}$ denotes the κ -th bit in the Gray code representation of symbol s_m . Then, the prior expectation $\mathbb{E}[x_i^{(n)}]$ and the variance $\text{Var}[x_i^{(n)}]$ of the symbol $x_i^{(n)}$ can be calculated as

$$\mathbb{E}[x_i^{(n)}] = \sum_{m=1}^M \Pr(x_i^{(n)} = s_m) s_m, \quad (15a)$$

$$\text{Var}[x_i^{(n)}] = \sum_{m=1}^M \Pr(x_i^{(n)} = s_m) \|s_m - \mathbb{E}[x_i^{(n)}]\|^2. \quad (15b)$$

Next, for each transmission stream n , the interference caused by all other streams is canceled from the observations \mathbf{y}_i , leading to

$$\tilde{\mathbf{y}}_{i,n} = \mathbf{y}_i - \sum_{n' \neq n} \hat{\mathbf{h}}_{n'} \mathbb{E}[x_i^{(n')}], \quad n = 1, \dots, N_t, \quad (16)$$

where $\hat{\mathbf{h}}_{n'}$ is the n' -th column of the channel estimate $\hat{\mathbf{H}}$. The posterior mean and variance of symbol $x_i^{(n)}$ are given by

$$\hat{x}_i^{(n)} = \mathbf{w}_n^H \tilde{\mathbf{y}}_{i,n}, \quad (17a)$$

$$\text{Var}[\hat{x}_i^{(n)}] = \mathbf{w}_n^H \left(\sum_{n' \neq n} \hat{\mathbf{h}}_{n'} \hat{\mathbf{h}}_{n'}^H \text{Var}[x_i^{(n')}] + \hat{\sigma}^2 \mathbf{I} \right) \mathbf{w}_n, \quad (17b)$$

where \mathbf{w}_n is the LMMSE equalizer

$$\mathbf{w}_n = \hat{\mathbf{h}}_n^H \left(\hat{\mathbf{H}} \mathbf{D}_n \hat{\mathbf{H}}^H + \hat{\sigma}^2 \mathbf{I} \right)^{-1} \quad (18)$$

for the channel estimate $\hat{\mathbf{H}}$, and matrix $\mathbf{D}_n \in \mathbb{C}^{N_t \times N_t}$ is diagonal with entries

$$[\mathbf{D}_n]_{n',n'} = \begin{cases} \text{Var}[x_i^{(n')}], & n' = n, \\ 1, & n' \neq n. \end{cases} \quad (19)$$

The posterior mean $\hat{x}_i^{(n)}$ and variance $\text{Var}[\hat{x}_i^{(n)}]$ in (15) are finally used to approximate the symbol posterior probability as

$$\hat{\Pr}(x_i^{(n)} = s_m | \hat{\mathbf{H}}, \hat{\sigma}^2, \mathbf{y}_i) = \frac{\exp\left(-\frac{\|\hat{x}_i^{(n)} - s_m\|^2}{\text{Var}[\hat{x}_i^{(n)}]}\right)}{\sum_{m'=1}^M \exp\left(-\frac{\|\hat{x}_i^{(n)} - s_{m'}\|^2}{\text{Var}[\hat{x}_i^{(n)}]}\right)}, \quad (20)$$

and the posteriori LLRs $L(c_k^{(n)} | \mathbf{Y})$ are acquired by marginalizing (20) over the symbol constellation as

$$L(c_k^{(n)} | \mathbf{Y}) = \ln \frac{\sum_{s_m \in \mathcal{S}_{(k \bmod q),1}} \hat{\Pr}(x_i^{(n)} = s_m | \hat{\mathbf{H}}, \hat{\sigma}^2, \mathbf{y}_i)}{\sum_{s_m \in \mathcal{S}_{(k \bmod q),0}} \hat{\Pr}(x_i^{(n)} = s_m | \hat{\mathbf{H}}, \hat{\sigma}^2, \mathbf{y}_i)}, \quad (21)$$

where $\mathcal{S}_{\kappa,1}$ and $\mathcal{S}_{\kappa,0}$ denote the subsets of constellation points where the κ -th bit of their Gray code representation is 1 and 0, respectively. Following this, the receiver performs the operations in (9)–(12), yielding the extrinsic LLRs $L_e(c_k^{(n)} | \mathbf{L}^{(n)})$. Finally, as illustrated by the dashed line in Fig. 3(a), the coded bits LLRs can be used to refine the estimates of $\hat{\mathbf{H}}$ and $\hat{\sigma}^2$ in subsequent turbo iterations [28], [33].

IV. ICL-BASED TURBO EQUALIZATION

In this section, we propose a soft channel equalization framework that leverages the ICL capability of sequence models to estimate the posterior LLRs of transmitted symbols without requiring explicit CSI. Specifically, as illustrated in Fig. 3(b), instead of relying on a two-stage approach with

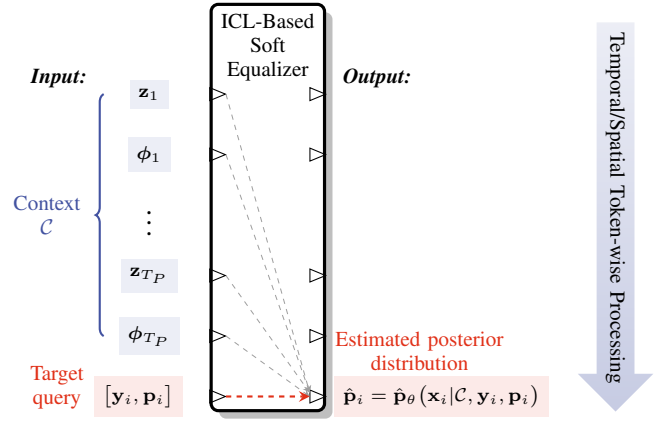


Fig. 4. Structure of an ICL-based soft equalizer.

channel estimation followed by linear equalization, the proposed ICL soft equalizer is prompted with a sequence of received–transmitted symbol pairs and directly estimates the new data symbols.

We start by describing the general operation of ICL-based soft equalization. Then, we detail the architecture of the underlying sequence model and its training procedure, including the tokenization and embedding strategy used to represent input–output examples, the formulation of the prompt structure, and the causal processing mechanism of the model. We also introduce two types of distinct model architectures that can be adopted to realize ICL soft equalization, as well as the supervised pre-training strategy used to optimize the prediction of posterior symbol distributions.

A. ICL-Based Soft Equalization

For each data symbol index i , the ICL soft equalizer processes a prompt sequence composed of the T_P pilots as well as the target query. The later concatenates the received symbol vector \mathbf{y}_i and a prior probability vector $\mathbf{p}_i \in \mathbb{R}^{M \cdot N_t}$. Accordingly, the prompt can be written as

$$\mathcal{P}_i = \left\{ \underbrace{\{\mathbf{z}_1, \phi_1, \dots, \mathbf{z}_{T_P}, \phi_{T_P}\}}_{\text{Context } \mathcal{C}}, \underbrace{[\mathbf{y}_i, \mathbf{p}_i]}_{\text{Target query}} \right\}, \quad (22)$$

where the pilots provide the context for the current task.

Unlike prior applications of ICL to wireless systems [11], [12], [14], [15], [23], [24], the proposed prompt (22) crucially incorporates the prior probability vector \mathbf{p}_i , enabling the soft equalizer to receive and process prior information about the distribution of the target symbol from the decoder. The prior vector \mathbf{p}_i is formatted as the concatenation of the per-antenna symbol probability mass functions (PMFs) as

$$\mathbf{p}_i = [\mathbf{p}_i^{(1)}, \dots, \mathbf{p}_i^{(N_t)}], \quad (23)$$

where each $\mathbf{p}_i^{(n)} \in \mathbb{R}^M$ represents the PMF over the constellation \mathcal{S} for the n -th transmit antenna, i.e.,

$$\mathbf{p}_i^{(n)} = [\Pr(x_i^{(n)} = s_1), \dots, \Pr(x_i^{(n)} = s_M)]. \quad (24)$$

As shown in Fig. 4, the $2T_P + 1$ vectors in the prompt \mathcal{P}_i are processed sequentially by a causal sequence model, which generates an output vector at each step based on the current

token and all preceding ones. In this formulation, the odd-numbered positions associated with received pilot symbols are implicitly treated as *queries*, and their corresponding known transmitted symbols at the following even-numbered positions act as *answers* (see Fig. 1(b)). The model effectively treats the prompt as an in-context supervised learning problem, predicting the transmitted symbol posterior conditioned on the past query–answer examples.

The final output vector produced by the sequence model, denoted as $\hat{\mathbf{p}}_i \in \mathbb{R}^{MN_t}$, is the only output of the soft equalizer in response to the input $[\mathbf{y}_i, \mathbf{p}_i]$. The outputs $\hat{\mathbf{p}}_i$ represents an estimate of the posterior distribution over the transmitted symbol vector \mathbf{x}_i , conditioned on the current observation \mathbf{y}_i , the prior \mathbf{p}_i , and the context \mathcal{C} given by the pilots. Accordingly, we write the output of the ICL-based soft equalizer as

$$\hat{\mathbf{p}}_i = \hat{\mathbf{p}}_\theta(\mathbf{x}_i | \mathcal{C}, \mathbf{y}_i, \mathbf{p}_i), \quad (25)$$

where the notation $\hat{\mathbf{p}}_\theta(\cdot)$ makes explicit the dependence of the equalizer on trainable parameters θ . The output $\hat{\mathbf{p}}_i$ of the ICL-based soft equalizer shares the same structure as the prior \mathbf{p}_i in (23), and hence can be written as

$$\hat{\mathbf{p}}_i = [\hat{\mathbf{p}}_i^{(1)}, \dots, \hat{\mathbf{p}}_i^{(N_i)}], \quad (26)$$

where $\hat{\mathbf{p}}_i^{(n)} \in \mathbb{R}^M$ with each entry corresponds to the estimated posterior probability

$$\hat{p}_{i,m}^{(n)} = \hat{\text{Pr}}(x_i^{(n)} = s_m | \mathcal{C}, \mathbf{y}_i, \mathbf{p}_i). \quad (27)$$

This output is finally converted to bitwise LLRs in the same way as (21), which are then passed to the channel decoder.

B. Tokenization and Embedding

The raw input vectors in the prompt \mathcal{P}_i in (22), are heterogeneous in both structure and dimensionality. They include complex-valued symbols and real-valued probabilities, which are not directly compatible with the input format expected by standard sequence models like Transformers. To address this problem, we perform a preliminary tokenization step that transforms each input into a fixed-dimensional real-valued vector, referred to as a *token vector*. Specifically, we construct a sequence of token vectors $\mathbf{t}_1, \dots, \mathbf{t}_{2T_P+1} \in \mathbb{R}^{(2+M)N_r \times 1}$ as

$$\begin{cases} \mathbf{t}_{2j-1} = [\Re(\mathbf{z}_j), \Im(\mathbf{z}_j), \frac{1}{M} \mathbf{1}_{N_r M}]^\top, & j \in \{1, \dots, T_P\}, \\ \mathbf{t}_{2j} = [\Re(\phi_j), \Im(\phi_j), \mathbf{0}_{N_r M}]^\top, & j \in \{1, \dots, T_P\}, \\ \mathbf{t}_{2T_P+1} = [\Re(\mathbf{y}_i), \Im(\mathbf{y}_i), \mathbf{p}_i]^\top, \end{cases} \quad (28)$$

where $\Re(\cdot)$ and $\Im(\cdot)$ denote the element-wise real and imaginary parts, respectively. Each token vector in (28) is formed by concatenating the real and imaginary components of a complex symbol vector with an additional segment that encodes prior knowledge. For the target query token \mathbf{t}_{2T_P+1} , this segment contains the prior distribution vector \mathbf{p}_i . In contrast, for the example query tokens, \mathbf{t}_{2j} for $j \in \{1, \dots, T_P\}$, we pad a uniform prior vector $\frac{1}{M} \mathbf{1}_{N_r M}$ to indicate the absence of prior information for the transmitted pilot symbols. Furthermore, for the example answer tokens \mathbf{t}_{2j} for $j \in \{1, \dots, T_P\}$, we zero-pad the vectors to match the dimension of the target query token \mathbf{t}_{2T_P+1} . This design ensures structural consistency across all tokens while preventing the model from relying

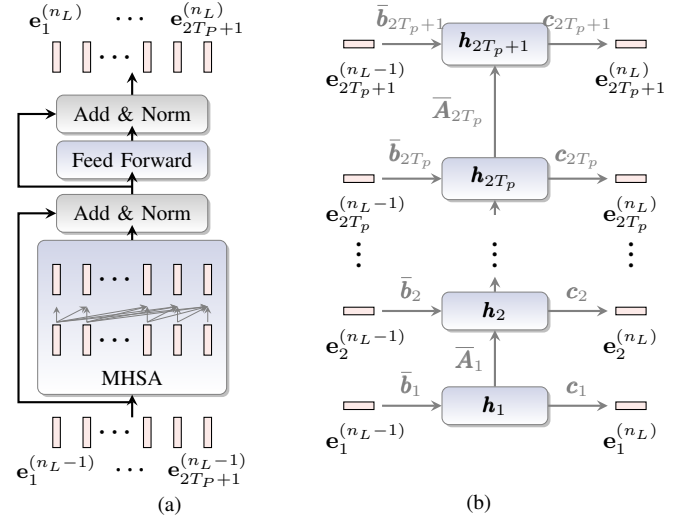


Fig. 5. Illustration of an arbitrary layer in the (a) Transformer (b) SSM model.

on prior information in the context. As such, the model is encouraged to learn the task-specific input-output mapping purely from the relational structure of the pilot examples.

Indexing the full sequence of token vectors as $\mathbf{t}_\ell \in \mathbb{R}^{(2+M)N_r \times 1}$, where $\ell = 1, \dots, 2T_P + 1$, each token vector is finally mapped into a D_E -dimensional *embedding vector* $\mathbf{e}_\ell^{(0)} \in \mathbb{R}^{D_E \times 1}$ as

$$\mathbf{e}_\ell^{(0)} = \mathbf{W}_{\text{emb}} \mathbf{t}_\ell, \quad (29)$$

where $\mathbf{W}_{\text{emb}} \in \mathbb{R}^{D_E \times (2+M)N_r}$ is a learnable weight matrix.

C. Sequence Models

The embedding sequence $\{\mathbf{e}_\ell^{(0)}\}_{\ell=1}^{2T_P+1}$ is fed into a causal sequence model for token-wise processing. We consider two model architectures as alternative backbones for this purpose: a Transformer decoder and an SSM. These two options offer complementary advantages: the former is better at capturing long-range dependencies, while the latter requires less computation and memory [34], [35].

1) *Transformer*: As shown in Fig. 5(a), the Transformer architecture processes all input token embeddings in parallel. We denote the collection of input embeddings as the matrix $\mathbf{E}^{(0)} \in \mathbb{R}^{D_E \times (2T_P+1)}$, which is defined as

$$\mathbf{E}^{(0)} = [\mathbf{e}_1^{(0)}, \mathbf{e}_2^{(0)}, \dots, \mathbf{e}_{2T_P+1}^{(0)}], \quad (30)$$

where each column corresponds to an embedding of a token in the prompt. The matrix $\mathbf{E}^{(0)}$ is fed into a stack of N_L Transformer decoder layers. Each layer produces an updated embedding matrix with the same dimensionality, which is denoted as $\mathbf{E}^{(1)}, \dots, \mathbf{E}^{(N_L)} \in \mathbb{R}^{D_E \times (2T_P+1)}$.

As summarized in Algorithm 1, each decoder layer takes as input an embedding matrix $\mathbf{E}^{(n_L-1)} \in \mathbb{R}^{D_E \times (2T_P+1)}$ in which each column corresponds to a token embedding. The input is first processed by a multi-head self-attention (MHSA) mechanism, which splits the embeddings into N_H attention heads of dimension D_H , such that $D_E = N_H D_H$. Within each head, a scaled dot-product attention operation is applied

Algorithm 1: Processing in a Transformer Decoder

Input: Embedding matrix from previous layer
 $\mathbf{E}^{(n_L-1)} \in \mathbb{R}^{D_E \times (2T_P+1)}$

Trainable Params: $\mathbf{W}_q, \mathbf{W}_k, \mathbf{W}_v \in \mathbb{R}^{D_E \times D_E}$,
 $\mathbf{W}_1 \in \mathbb{R}^{D_F \times D_E}, \mathbf{W}_2 \in \mathbb{R}^{D_E \times D_F}$,
 $\epsilon_1 \in \mathbb{R}^{D_F \times 1}, \epsilon_2 \in \mathbb{R}^{D_E \times 1}$

Output: Updated embeddings $\mathbf{E}^{(n_L)} \in \mathbb{R}^{D_E \times (2T_P+1)}$

- 1 **for each head** $h = 1, \dots, N_H$ **do in parallel**
- 2 $\mathbf{Q}_h \leftarrow \mathbf{W}_h^Q \mathbf{E}^{(n_L-1)} \in \mathbb{R}^{D_H \times (2T_P+1)}$;
- 3 $\mathbf{K}_h \leftarrow \mathbf{W}_h^K \mathbf{E}^{(n_L-1)} \in \mathbb{R}^{D_H \times (2T_P+1)}$;
- 4 $\mathbf{V}_h \leftarrow \mathbf{W}_h^V \mathbf{E}^{(n_L-1)} \in \mathbb{R}^{D_H \times (2T_P+1)}$;
- 5 $\mathbf{A}_h \leftarrow \text{Softmax} \left(\frac{\mathbf{Q}_h^\top \mathbf{K}_h}{\sqrt{D_H}} + \mathbf{M} \right) \mathbf{V}_h^\top \triangleright$ (MHSA);
- 6 **end**
- 7 Concatenate all \mathbf{A}_h and project to get MHSA output:
 $\mathbf{A} = [\mathbf{A}_1, \dots, \mathbf{A}_{N_H}]^\top \in \mathbb{R}^{D_E \times (2T_P+1)}$;
- 8 Apply residual connection and layer normalization:
 $\mathbf{E}_{\text{mhsa}} \leftarrow \text{LayerNorm}(\mathbf{A} + \mathbf{E}^{(n_L-1)})$;
- 9 $\mathbf{F} \leftarrow \text{GeLU}(\mathbf{W}_1 \mathbf{E}_{\text{mhsa}} + \epsilon_1)$;
- 10 $\mathbf{E}^{(n_L)} \leftarrow \text{LayerNorm}(\mathbf{W}_2 \mathbf{F} + \epsilon_2 + \mathbf{E}_{\text{mhsa}}) \triangleright$ (FFN);
- 11 **return** $\mathbf{E}^{(n_L)}$

to capture contextual dependencies. To preserve the causal structure, a mask matrix $\mathbf{M} \in \mathbb{R}^{(2T_P+1) \times (2T_P+1)}$ is added to the attention logits to prevent each token from attending to future positions:

$$M_{i,j} = \begin{cases} 0, & j \leq i \\ -\infty, & j > i \end{cases} \quad (31)$$

The outputs of all heads are concatenated and projected back to the embedding space, followed by residual connections and layer normalization. A position-wise feedforward network (FFN) is then applied to each token embedding independently, which consists of two linear layers with a GeLU activation in between. Another residual connection and normalization layer completes the decoder block.

At the N_L -th layer, the output embedding matrix is denoted as $\mathbf{E}^{(N_L)} = [\mathbf{e}_1^{(N_L)}, \dots, \mathbf{e}_{2T_P+1}^{(N_L)}]$, which is formatted as the set of output embeddings produced by the sequence model.

2) *State-Space Model*: Unlike the Transformer architecture, which processes all the inputs in parallel through an attention mechanism, as illustrated in Fig. 5(b), the SSM architecture operates sequentially over the input embeddings. A standard continuous-time scalar-input SSM maps an input $u(t) \in \mathbb{R}$ to an output $o(t) \in \mathbb{R}$ through a hidden state $\mathbf{h}(t) \in \mathbb{R}^{D_h \times 1}$ via the differential equation and output relationship

$$\frac{d\mathbf{h}}{dt} = \mathbf{A}\mathbf{h}(t) + \mathbf{b}u(t), \quad \text{and} \quad o(t) = \mathbf{c}\mathbf{h}(t), \quad (32)$$

respectively, where $\mathbf{A} \in \mathbb{R}^{D_h \times D_h}$, $\mathbf{b} \in \mathbb{R}^{D_h \times 1}$, and $\mathbf{c} \in \mathbb{R}^{1 \times D_h}$. Discretizing with step size Δ yields the discrete-time system [35]

$$\mathbf{h}_t = \bar{\mathbf{A}}\mathbf{h}_{t-1} + \bar{\mathbf{b}}u_t, \quad (33a)$$

$$o_t = \mathbf{c}\mathbf{h}_t, \quad (33b)$$

Algorithm 2: Processing in a Selective SSM Layer

Input: $\mathbf{e}_1^{(n_L-1)}, \dots, \mathbf{e}_{2T_P+1}^{(n_L-1)} \in \mathbb{R}^{D_E \times 1}$

Output: $\mathbf{e}_1^{(n_L)}, \dots, \mathbf{e}_{2T_P+1}^{(n_L)} \in \mathbb{R}^{D_E \times 1}$

Trainable Params: $\mathbf{W}_b, \mathbf{W}_c \in \mathbb{R}^{D_h \times D_E}$, $\mathbf{w}_\Delta \in \mathbb{R}^{1 \times D_E}$,
 $\epsilon_b, \epsilon_c, \epsilon_\Delta \in \mathbb{R}^{D_h \times 1}$,
 $\mathbf{W}_g, \mathbf{W}_u \in \mathbb{R}^{D_E \times D_E}$

- 1 **for** $\ell = 1$ **to** $2T_P + 1$ **do**
- 2 $\mathbf{b}_\ell \leftarrow \mathbf{W}_b \mathbf{e}_\ell^{(n_L-1)} + \epsilon_b \in \mathbb{R}^{D_h \times 1}$
 \triangleright Calculate input-dependent state transition vector;
- 3 $\mathbf{c}_\ell \leftarrow \mathbf{W}_c \mathbf{e}_\ell^{(n_L-1)} + \epsilon_c \in \mathbb{R}^{D_h \times 1}$
 \triangleright Calculate input-dependent output mapping vector;
- 4 $\Delta_\ell \leftarrow \text{Softplus}(\epsilon_\Delta + \mathbf{w}_\Delta \mathbf{e}_\ell^{(n_L-1)}) \mathbf{1}_{D \times 1} \in \mathbb{R}^{D_h \times 1}$
 \triangleright Calculate input-dependent discretization step;
- 5 **for** $d = 1$ **to** D_E **do in parallel**
- 6 $\bar{\mathbf{A}}_{\ell,d} = (\mathbf{I} - \Delta_{\ell,d}/2 \cdot \mathbf{A})^{-1} (\mathbf{I} + \Delta_{\ell,d}/2 \cdot \mathbf{A})$
 \triangleright Discretization (34a);
- 7 $\bar{\mathbf{b}}_{\ell,d} = (\mathbf{I} - \Delta_{\ell,d}/2 \cdot \mathbf{A})^{-1} \Delta_{\ell,d} \mathbf{b}_\ell$
 \triangleright Discretization (34b);
- 8 $\mathbf{h}_{\ell,d} \leftarrow \begin{cases} \bar{\mathbf{A}}_{\ell,d} \mathbf{h}_{\ell-1,d} + \bar{\mathbf{b}}_{\ell,d} u_{\ell,d}, & \ell > 1 \\ \bar{\mathbf{b}}_{\ell,d} \mathbf{e}_{\ell,d}^{(n_L-1)}, & \ell = 1 \end{cases}$
 \triangleright State update (33a);
- 9 $e'_{\ell,d} \leftarrow \mathbf{c}_\ell \mathbf{h}_{\ell,d} \triangleright$ Scalar SSM output (33b);
- 10 **end**
- 11 $\mathbf{e}'_\ell = [e'_{\ell,1}, \dots, e'_{\ell,D_E}]^\top \in \mathbb{R}^{D_E \times 1}$;
- 12 $\mathbf{e}_\ell^{(n_L)} = \text{Sigmoid}(\mathbf{W}_g \mathbf{e}'_\ell) \odot (\mathbf{W}_u \mathbf{e}'_\ell) \triangleright$ (GLU);
- 13 **end**

with

$$\bar{\mathbf{A}} = \left(\mathbf{I} - \frac{\Delta}{2} \mathbf{A} \right)^{-1} \left(\mathbf{I} + \frac{\Delta}{2} \mathbf{A} \right), \quad (34a)$$

$$\bar{\mathbf{b}} = \left(\mathbf{I} - \frac{\Delta}{2} \mathbf{A} \right)^{-1} \Delta \mathbf{b}, \quad (34b)$$

where vectors \mathbf{b} and \mathbf{c} are trainable. Via the updates (33), SSMs support both parallel sequence processing via convolutional training and linear-time recurrent inference [35]. The matrix \mathbf{A} is typically fixed as a constant lower-triangular matrix to ensure a normal-plus-low-rank structure for efficient computation [35].

A notable variant of SSM is the *selective SSM* architecture, also known as *Mamba* [36]. Selective SSM introduces input-dependent vectors \mathbf{b}_t , \mathbf{c}_t , and a time-varying step size Δ_t . These components enable token-aware recurrent computation by allowing dynamic modulation of hidden state updates based on the input. This selective processing enhances the model's capability for ICL [37].

In the SSM-based variant of our ICL soft equalization framework, the input embeddings $\{\mathbf{e}_1^{(0)}, \dots, \mathbf{e}_{2T_P+1}^{(0)}\}$ are sequentially processed across N_L *selective SSM* layers. As shown in Fig. 5(b), at the ℓ -th step, the n_L -th layer takes $\mathbf{e}_\ell^{(n_L-1)}$ as input, updates its hidden state, and produces the updated embedding $\mathbf{e}_\ell^{(n_L)}$.

The detailed computing process is described in Algorithm 2. For each time step ℓ , the vectors \mathbf{b}_ℓ and \mathbf{c}_ℓ are computed via trainable linear projections applied to the input token vector $\mathbf{e}_\ell^{(n_L-1)}$. Furthermore, a step size vector Δ_ℓ is obtained by applying the $\text{Softplus}(\cdot)$ function to the sum of a trainable bias vector ϵ_Δ and the output of a trainable scalar linear function

applied to $\mathbf{e}_\ell^{(n_L-1)}$. Subsequently, each scalar component of the input embedding $\mathbf{e}_\ell^{(n_L-1)}$ is processed independently by a corresponding SSM submodel. Each entry $\Delta_{\ell,d}$ in $\mathbf{\Delta}_\ell$ defines the step size used by the d -th parallel SSM submodel. The scalar outputs of the submodels are then concatenated to form the output vector of the SSM. This vector is passed through a gated linear unit (GLU) to allow the model to dynamically modulate information flow per time step. This results in the final output of the selective SSM layer, denoted $\mathbf{e}_\ell^{(n_L)}$.

After $2T_P + 1$ time steps, the $2T_P + 1$ output embedding vectors $\mathbf{E}^{(N_L)} = [\mathbf{e}_1^{(N_L)}, \dots, \mathbf{e}_{2T_P+1}^{(N_L)}]$ from the N_L -th layer are collected, which serve as the final output of the model.

D. Multi-Head Classifier

The multi-head classifier forms the final layer of the ICL soft equalizer, mapping the output embeddings $\mathbf{E}^{(N_L)}$ from either Transformer or SSM sequence models to posterior symbol probability distributions. The classifier comprises N_t parallel fully connected heads, each responsible for producing a probability distribution over the M constellation points for one transmit antenna.

For each token position $\ell \in \{1, \dots, 2T_P + 1\}$, the corresponding output embedding $\mathbf{e}_\ell^{(N_L)} \in \mathbb{R}^{D_E}$ is transformed into a concatenated output vector $\mathbf{o}_\ell \in \mathbb{R}^{N_t M}$ as

$$\mathbf{o}_\ell = \begin{bmatrix} \text{Softmax}(\mathbf{W}_O^{(1)} \mathbf{e}_\ell^{(N_L)} + \boldsymbol{\epsilon}_O^{(1)})^\top \\ \vdots \\ \text{Softmax}(\mathbf{W}_O^{(N_t)} \mathbf{e}_\ell^{(N_L)} + \boldsymbol{\epsilon}_O^{(N_t)})^\top \end{bmatrix}, \quad (35)$$

where $\mathbf{W}_O^{(n)} \in \mathbb{R}^{M \times D_E}$ and $\boldsymbol{\epsilon}_O^{(n)} \in \mathbb{R}^{M \times 1}$ are trainable parameters for the n -th output head. The output vector \mathbf{o}_ℓ consists of N_t segments, each of length M , with each segment specialized for one transmit antenna.

At inference phase, only the final token's output \mathbf{o}_{2T_P+1} is used, which corresponds to the posterior estimate

$$\hat{\mathbf{p}}_i = \mathbf{o}_{2T_P+1}, \quad (36)$$

as defined in Sec. IV-A.

V. PRE-TRAINING OF ICL-BASED SOFT EQUALIZER

The previous section has introduced the operation of the proposed ICL-based soft equalizer. This section describes the offline pre-training phase, in which the parameters θ of the ICL-based soft equalizer are optimized using data from multiple tasks.

A. Data Generation

Pre-training leverages a dataset comprising data from a subset $\mathcal{T}_{\text{train}}$ of N_{train} simulated task instances drawn i.i.d. from a pre-training task distribution \mathcal{D}_τ . The training tasks, denoted as

$$\mathcal{T}_{\text{train}} = \{\tau_n\}_{n=1}^{N_{\text{train}}} \sim \mathcal{D}_\tau^{\otimes N_{\text{train}}}, \quad (37)$$

are such that each task $\tau_n = \{\mathbf{H}_n, \sigma_n^2, \mathcal{Q}_n\}$ in (8) specifies a distinct communication link.

Unlike the inference phase, where context and target query tokens have different structures, training is performed using

prompt sequences of interleaved query-answer pairs. Specifically, each training prompt consists of T_{train} such pairs, and is structured as

$$\mathcal{P}_{\text{train}} = \left\{ \underbrace{[\mathbf{y}_1, \mathbf{p}_1]}_{\text{query 1}}, \underbrace{\mathbf{x}_1}_{\text{answer 1}}, \dots, \underbrace{[\mathbf{y}_{T_{\text{train}}}, \mathbf{p}_{T_{\text{train}}}]}_{\text{query } T_{\text{train}}}, \underbrace{\mathbf{x}_{T_{\text{train}}}}_{\text{answer } T_{\text{train}}} \right\}. \quad (38)$$

For each symbol index $j \in \{1, \dots, T_{\text{train}}\}$ and each transmit antenna $n \in \{1, \dots, N_t\}$, we first sample the prior PMF $\mathbf{p}_j^{(n)} \in \mathbb{R}^M$ independently from a Dirichlet distribution

$$\mathbf{p}_j^{(n)} \sim \text{Dir}(\boldsymbol{\beta}), \quad (39)$$

where $\boldsymbol{\beta} \in \mathbb{R}^M$ is the concentration parameter vector. In our implementation, we use $\boldsymbol{\beta} = \mathbf{1}_M$, which ensures uniform sampling over the probability simplex and maximizes diversity in prior distributions. Higher values of $\boldsymbol{\beta}$ yield priors with higher entropy, while smaller values are associated with sparser and lower entropy priors. We do not claim the optimality of the choice $\boldsymbol{\beta} = \mathbf{1}_M$.

Given the prior $\mathbf{p}_j^{(n)}$, the transmitted symbol vectors $\mathbf{x}_j = [x_j^{(1)}, \dots, x_j^{(N_t)}] \in \mathcal{S}^{N_t}$ are obtained by sampling each symbol $x_j^{(n)}$ independently from the PMF $\mathbf{p}_j^{(n)}$ with support given by the M -QAM constellation. The sampled symbols are then transmitted and received according to the link model (6b), which is parameterized by a random task $\tau \sim \mathcal{U}(\mathcal{T}_{\text{train}})$, resulting in the corresponding received symbols \mathbf{y}_j .

Finally, the j -th query vector $[\mathbf{y}_j, \mathbf{p}_j]$ is formed by concatenating each received symbol \mathbf{y}_j with its associated prior vector $\mathbf{p}_j = [\mathbf{p}_j^{(1)}, \dots, \mathbf{p}_j^{(N_t)}] \in \mathbb{R}^{N_t M}$. The corresponding answer is the ground-truth transmitted vector \mathbf{x}_j . Together, these form the interleaved training prompt defined in (38).

B. Parameter Optimization

As illustrated in Fig. 6, each training prompt undergoes the same tokenization and forward computation steps described in Sec. IV, resulting in a sequence of output vectors $\mathbf{o}_1, \mathbf{o}_2, \dots, \mathbf{o}_{2T_{\text{train}}} \in \mathbb{R}^{M N_t}$.

Unlike the inference stage, where only the final output is used for prediction, during the training stage all output vectors at odd indices are used to compute the model's estimation error and optimize its parameters. For convenience, we redefine them as

$$\hat{\mathbf{p}}_j = \mathbf{o}_{2j-1}, \quad j = 1, 2, \dots, T_{\text{train}}. \quad (40)$$

The model, parameterized by θ , is then evaluated using a weighted cross-entropy loss:

$$\mathcal{L}_\theta = - \sum_{j=1}^{T_{\text{train}}} w_j \sum_{n=1}^{N_t} \sum_{m=1}^M \delta(m, \text{idx}_M(x_j^{(n)})) \log \hat{p}_{j,(n-1)M+m}, \quad (41)$$

where $\delta(\cdot, \cdot)$ is the Kronecker delta function, and $\text{idx}_M(x_j^{(n)}) \in \{1, \dots, M\}$ denotes the index of the transmitted symbol $x_j^{(n)}$, which follows the Gray code ordering of the constellation in the M -QAM constellation \mathcal{S} .

The coefficient w_j is introduced to assign lower weights to early predictions and higher weights to later ones. This is aligned with the principle of ICL, which expects the model

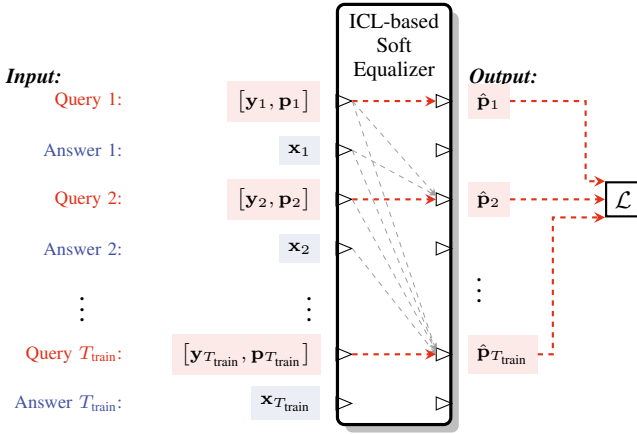


Fig. 6. Illustration of the pre-training process for ICL-based equalization.

to make increasingly accurate predictions as more context becomes available. Specifically, the weight w_j is computed as [38]

$$w_j = \frac{\log(1 + \lambda_j)}{\sum_{j'=1}^{T_{\text{train}}} \log(1 + \lambda_{j'})}, \quad (42)$$

where λ is a hyperparameter controlling the growth rate of w_j . A larger λ places more weight on later predictions, encouraging the model to progressively refine its inferences as additional context accumulates. In this work, we set $\lambda = 0.5$.

The model parameters θ are finally optimized by minimizing the expected loss over randomly sampled training sequences as

$$\arg \min_{\theta} \sum_{\tau \in \mathcal{T}_{\text{train}}} \mathbb{E}_{\mathcal{P}_{\text{train}} \sim \mathcal{D}_{\mathcal{P}|\tau}} [\mathcal{L}_{\theta}]. \quad (43)$$

In our implementation, optimization is performed using the AdamW optimizer through backpropagation, with a cosine-annealed learning rate schedule [39].

VI. NUMERICAL EVALUATIONS

In this section, we evaluate the performance of the proposed ICL soft equalization in a turbo equalization framework.

A. Simulation Setup

We consider a MIMO system with $N_t = N_r = 4$ antennas. At the transmitter side, information bits are generated i.i.d. from a uniform binary source and encoded using a 5G new radio (NR) low-density parity-check (LDPC) encoder following the 3GPP 38.212 including rate-matching [40]. The codeword stream for each transmit antenna is subsequently interleaved using a per-antenna independent random interleaver. The resulting interleaved codewords are then modulated using either 4-QAM (QPSK) or 16-QAM schemes, i.e., $M \in \{4, 16\}$.

The communication channel is modeled as a MIMO Rayleigh fading channel with additive Gaussian noise, where each entry of the channel matrix \mathbf{H} is assumed to be i.i.d. drawn from $\mathcal{CN}(0, 1)$ and distinct from those used for generating training data. At the receiver side, a mid-rise uniform quantizer, with clipping boundaries at $l_{\min} = -4$ and $l_{\max} = 4$, quantizes the received signal as (6). Thus, the front end setting is varied by modifying only the resolution B . For error correction, we employ a generic belief propagation (BP)

decoder implementing the flooding message passing algorithm [41], and the maximum number of BP iterations is set to 20.

B. Benchmarks

To evaluate the performance of the proposed ICL-based soft equalizer, we compare it against the following baselines:

1) *RLS-LMMSE-PIC*: We implement a state-of-the-art model-based baseline that integrates the RLS-based channel tracking approach from [42] with the LMMSE-PIC soft equalization algorithm introduced in [4]. Architecturally, the baseline follows the structure shown in Fig. 3(a), where reliable soft symbol vectors mapped from decoder posterior LLRs are fed back as additional training data for iterative channel estimation. This setup allows the equalizer to progressively refine its channel estimate during turbo iterations.

2) *LMMSE-PIC with Bussgang Gain (BLMMSE-PIC) and Perfect CSI*: This baseline applies the same BLMMSE-PIC soft equalization algorithm as in RLS-LMMSE-PIC, but is provided with perfect knowledge of the channel matrix \mathbf{H} and noise variance σ^2 . Additionally, it incorporates the Bussgang gain to account for the distortion introduced by the quantized observations [43]. This baseline helps isolate the performance degradation caused by imperfect channel estimation and non-linear modeling errors in RLS-LMMSE-PIC.

3) *Optimal Baseline — MAP Equalization with Perfect CSI*: This idealized baseline computes the maximum a posteriori (MAP) estimate of the transmitted symbol vector assuming perfect knowledge of \mathbf{H} and σ^2 . It serves as a lower bound on detection error.

C. Configuration Settings

The proposed ICL soft equalization framework is implemented using two different network architectures: *ICL-T*, which adopts a Transformer-based architecture built on a GPT-2 backbone [44], and *ICL-S*, which uses an SSM architecture based on the Mamba backbone [36]. Unless otherwise specified, all models used in the simulations follow the configurations in Table I and are trained on sequences consisting of $T_{\text{train}} = 40$ query-answer token pairs. The training sequences are generated according to the procedures described in Sec. V, using tasks independently drawn from a pre-training task pool $\mathcal{T}_{\text{train}}$ comprising $N_{\text{train}} = 2^{15} = 32,768$ unique combinations.

TABLE I
ARCHITECTURE-SPECIFIC PARAMETERS FOR ICL-T AND ICL-S

ICL-T		ICL-S	
Parameter	Value	Parameter	Value
Backbone	GPT-2 [44]	-	Mamba [36]
# layers (N_L)	4	-	4
Embedding dim. (D_E)	256	-	256
Max. sequence length	80	State size	16
Attention heads (N_H)	8	Kernel size	4
FFN hidden dim	1024	MLP hidden dim	1024
Total parameters	16.07 M	Total parameters	6.38 M

During pre-training, task instances are sampled from a joint distribution defined as $\mathcal{D}_{\tau} = \mathcal{D}_H \otimes \mathcal{D}_{\sigma^2} \otimes \mathcal{D}_B$, where $\mathcal{D}_H = \mathcal{CN}(0, \mathbf{I})$ represents i.i.d. Rayleigh fading channels,

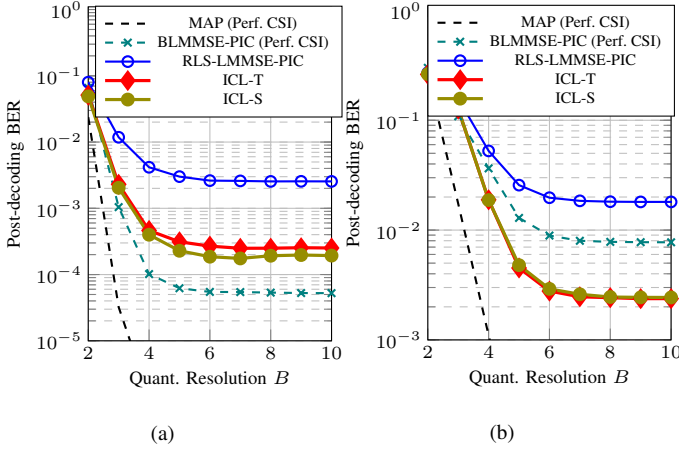


Fig. 7. Post-decoding BER versus quantization bit width under (a) 4-QAM, SNR=5 dB and (b) 16-QAM, SNR=15 dB. The results are evaluated after the first turbo iteration with $T_P = 16$.

$\mathcal{D}_{\sigma^2} = \mathcal{U}[10^{-3}, 1]$ is a uniform distribution over noise variances corresponding to SNR levels between 0 dB and 30 dB, and $\mathcal{D}_B = \mathcal{U}(\{1, 2, \dots, 32\})$ denotes a uniform distribution over the number of active non-zero symbols.

The model is trained using a mini-batch size of 128 prompts. Each epoch consists of 200 iterations with freshly sampled mini-batches, and training is conducted for a total of 2000 epochs. The peak learning rate is set to 1×10^{-4} .

To evaluate generalization, we ensure that the test data is generated from a disjoint task set $\mathcal{T}_{\text{test}}$, i.e., $\mathcal{T}_{\text{test}} \cap \mathcal{T}_{\text{train}} = \emptyset$.

D. Impact of Quantization Resolution

We begin by evaluating the performance of the proposed ICL soft equalization framework under finite-resolution quantization. To isolate the impact of quantization, we fix the SNR at moderate levels, specifically, 5 dB for 4-QAM and 15 dB for 16-QAM. We consider only the first turbo iteration, where no prior information from the decoder is available. The pilot length is set to $T_P = 16$, and the quantization resolution is varied from $B = 2$ to $B = 10$.

Fig. 7(a) presents the post-decoding bit error rate (BER) under 4-QAM. The results show that both ICL-T and ICL-S consistently outperform the RLS-LMMSE-PIC baseline across all quantization levels, with ICL-S achieving slightly superior performance. The ICL-based equalizers maintain strong detection accuracy even in the low-resolution regime. For instance, at 4-bit quantization, both ICL-T and ICL-S achieve a BER under 5×10^{-4} , while RLS-LMMSE-PIC achieves a BER equal to 4×10^{-3} . Similar trends are observed for 16-QAM in Fig. 7(b), where both ICL-T and ICL-S reach a BER of approximately 5×10^{-3} under 5-bit quantization. This is in contrast to the RLS-LMMSE-PIC baseline, which achieves a BER of only 2×10^{-2} . These results highlight the robustness of ICL soft equalization in systems equipped with low-bit ADCs.

Under 4-QAM, both ICL-T and ICL-S approach the performance of BLMMSE-PIC with perfect CSI but do not exceed it. In contrast, under 16-QAM, the ICL-based methods outperform the BLMMSE-PIC baseline with perfect CSI and achieve

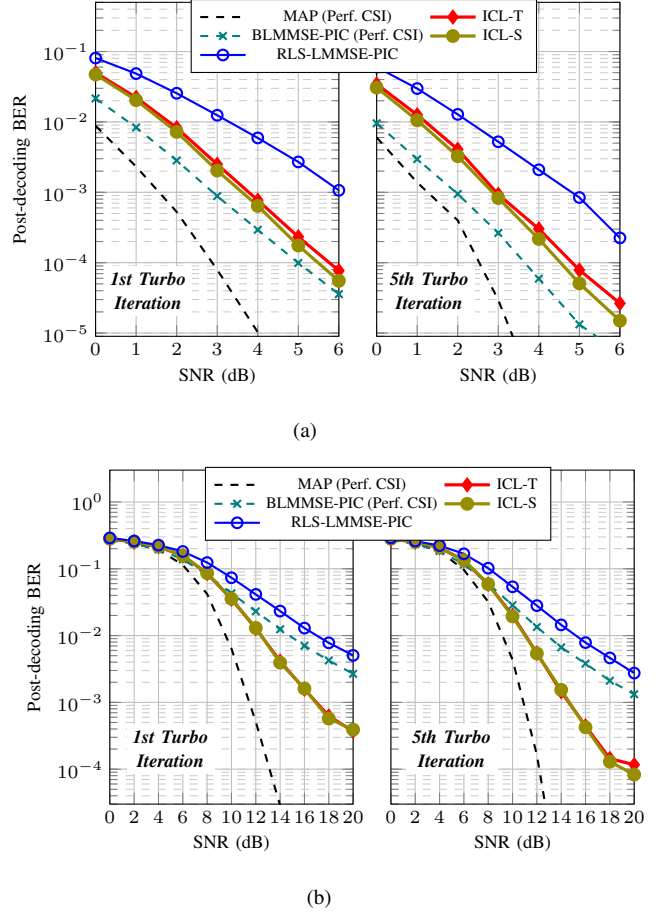


Fig. 8. Post-decoding BER versus SNR under (a) 4-QAM, $B = 6$ and (b) 16-QAM, $B = 8$. In each subfigure, the left panel shows the results after the 1st turbo iteration, while the right panel shows the results after the 5th turbo iteration.

performance closer to that of the MAP detector. This suggests that ICL is capable of implicitly learning the nonlinear and discrete characteristics of higher-order modulations from data, which gives it a clear advantage over BLMMSE-PIC, whose design relies on Gaussian assumptions and linearity. In the case of 4-QAM, the detection problem is inherently simpler, and BLMMSE-PIC with perfect CSI is already close to optimal, which limits the potential gains from ICL.

As the quantization resolution increases, the BER of all methods improves and gradually saturates, with marginal performance gains beyond $B = 6$ for 4-QAM and $B = 8$ for 16-QAM. In this high-resolution regime, ICL-T and ICL-S consistently maintain roughly one order of magnitude lower BER compared to RLS-LMMSE-PIC, which highlights the ability of the ICL-equalizer to achieve lower BER in cases of short pilot sequences.

E. Effect of the SNR

We evaluate the post-decoding BER of the proposed ICL-T and ICL-S models under both 4-QAM and 16-QAM modulation schemes, and compare them with baseline algorithms, as a function of the SNR. The quantization resolutions are set to $B = 6$ for 4-QAM and $B = 8$ for 16-QAM, as justified

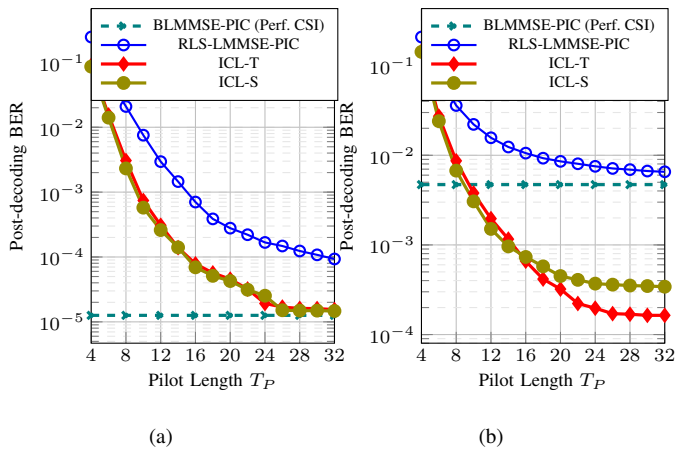


Fig. 9. Post-decoding BER versus pilot length under (a) 4-QAM, SNR=5 dB, $B = 6$ and (b) 16-QAM, SNR=15 dB, $B = 8$. The results are evaluated at the fifth turbo iteration with $T_P = 16$.

in Sec. VI-D. Each model is evaluated after the first and fifth turbo decoding iterations to assess its ability to refine soft symbol estimates using decoder feedback.

Fig. 8(a) shows the results for 4-QAM. Both ICL-T and ICL-S achieve similar performance and exhibit significant BER reduction between the first and fifth turbo iterations, demonstrating their ability to refine equalization through decoder-provided prior information. Across all SNR levels, both ICL variants consistently outperform the practical RLS-LMMSE-PIC baseline, and closely approach the performance of BLMMSE-PIC with perfect CSI.

For 16-QAM, shown in Fig. 8(b), both ICL-T and ICL-S outperform the RLS-LMMSE-PIC baseline across the full SNR range. Notably, in the high-SNR regime, ICL-based soft equalization begins to surpass the BLMMSE-PIC baseline with perfect CSI. This is attributed to the modeling limitations of BLMMSE-PIC, which relies on a Gaussian prior and linearity. As the SNR increases, the Gaussian approximation becomes the dominant performance bottleneck, particularly for higher-order QAM, where symbol distributions are discrete and highly structured. In contrast, the ICL framework learns these discrete characteristics directly from data, efficiently approaching the MAP detector.

F. Effect of the Number of Pilot Symbols

We now evaluate the effect of the pilot length T_P on the post-decoding BER for both ICL-based models and the baseline algorithms at the fifth turbo iteration. The quantization resolution is set to $B = 6$ for 4-QAM and $B = 8$ for 16-QAM. The SNR is fixed at 5 dB for 4-QAM and 15 dB for 16-QAM. The pilot length T_P is varied from 4 to 32.

Fig. 9(a) shows the results for 4-QAM. All channel-agnostic methods benefit from increasing pilot length T_P . Notably, both ICL models outperform RLS-LMMSE-PIC even when using significantly fewer pilots. For example, the BER achieved by ICL with only $T_P = 16$ context pilots is lower than that of BLMMSE-PIC using $T_P = 32$ pilots for CSI estimation. This demonstrates that ICL-based soft equalization can quickly

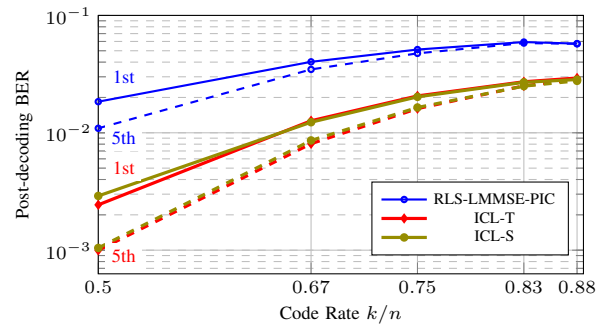


Fig. 10. Post-decoding BER versus LDPC code rate, evaluated at the 1st (solid lines) and 5th (dashed lines) turbo iterations. The results are obtained under 16-QAM, with SNR=15 dB, $B = 8$, and $T_P = 16$.

adapt to the channel with limited pilot examples. ICL-T and ICL-S perform comparably, and approach the performance of BLMMSE-PIC with perfect CSI as T_P increases.

For 16-QAM (Fig. 9(b)), RLS-LMMSE-PIC converges toward the performance of the BLMMSE-PIC baseline with perfect CSI as T_P increases. However, both ICL-T and ICL-S exhibit increasingly stronger performance with increasing T_P and surpass the BLMMSE-PIC baseline with perfect CSI when $T_P \geq 10$, despite not relying on explicit channel estimation. These results highlight the advantage of ICL models in adapting to both the channel and the discrete symbol structure from context examples. In contrast, linear model-based algorithms suffer from an inherent performance bottleneck caused by the mismatch between their assumed Gaussian priors and the true nonlinear, discrete modulation, even when CSI is accurately estimated.

G. Impact of Channel Code Rate

We further evaluate the performance of ICL soft equalization by varying the LDPC code rates. As shown in Fig. 10, the post-decoding BER is measured after the first and fifth turbo decoding iterations, with the code rate varying from 1/2 to 7/8. The behaviors of all methods align with classical turbo equalization theory, where high BER gain can be achieved through turbo iterations at lower code rates because the added redundancy allows greater room for iterative refinement. As the code rate increases, the BER naturally rises due to reduced error protection, and the relative improvement from turbo iterations becomes less significant. These results further validate the ability of ICL soft equalization to effectively incorporate prior information provided by the decoder. Still, both ICL-T and ICL-S consistently outperform RLS-LMMSE-PIC across all coding rates.

H. Generalization Across Training Regimes

We now evaluate the generalization performance of the ICL models as a function of training data diversity, quantified by the number of unique tasks N_{train} used to generate the training sequences. Specifically, we train multiple instances of ICL-T and ICL-S from scratch on datasets synthesized from different values of N_{train} , which range exponentially from $N_{\text{train}} = 2^6 = 64$ up to $N_{\text{train}} = 2^{15} = 32,768$.

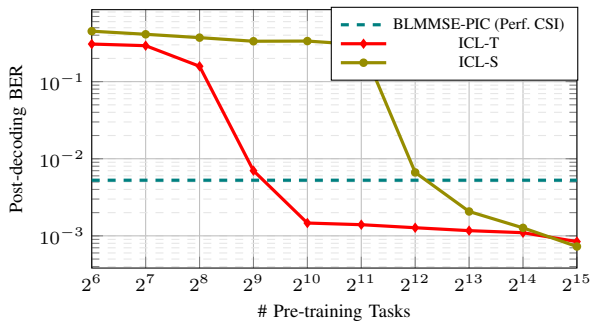


Fig. 11. Post-decoding BER performance for ICL-T and ICL-S models trained on varying numbers of pre-training tasks N_{train} compared with the BLMMSE-PIC algorithm with perfect CSI. The results are evaluated at the fifth turbo iteration under 16-QAM, with SNR=15 dB, $B = 8$, and $T_P=16$.

Fig. 11 presents the BER results for both ICL-T and ICL-S compared against the BLMMSE-PIC baseline with perfect CSI, evaluated under the same signal configuration and all after five turbo iterations. The ICL-T demonstrates strong generalization capability, outperforming the BLMMSE-PIC baseline even when trained on relatively homogeneous data (e.g., with only $N_{\text{train}} = 2^{10} = 1,024$ pre-training tasks). This fast generalization can be attributed to the non-sequential input structure of Transformers, which allows the model to more effectively extract and utilize link-related information from the context during inference.

In contrast, the ICL-S shows limited performance when trained on low-diversity datasets. However, its performance improves significantly with increasing training diversity, surpassing BLMMSE-PIC once $N_{\text{train}} \geq 2^{13} = 8,192$. This suggests that the state-space architecture requires a broader range of training conditions to learn effective context-dependent representations due to its implicit compression mechanisms.

I. Model Size and Computational Efficiency

We finally evaluate model size and number of floating-point operations (FLOPs) required during inference for different ICL-T and ICL-S models using the standard PyTorch profiler. We consider 16-QAM modulation and SNR = 15 dB with $B = 8$ and $T_P = 16$. To provide a fair and informative comparison, all models are trained on the same dataset using identical hyperparameters.

For the Transformer-based ICL-T architecture, we adopt a standard key-value caching mechanism similar to that used in autoregressive models [45]. Specifically, the attention cache for the pilot context is precomputed once and reused, allowing the model to process only the new token representing the data symbol vector during inference. This reduces the computational complexity per symbol vector from quadratic to linear with respect to the pilot length, while increasing memory usage from linear to quadratic due to the cached attention keys and values.

The SSM-based ICL-S architecture maintains a constant computational and memory complexity per data symbol vector. After the pilot context \mathcal{C} is processed once, its resulting hidden state \mathbf{h} is cached and reused. Each subsequent data symbol

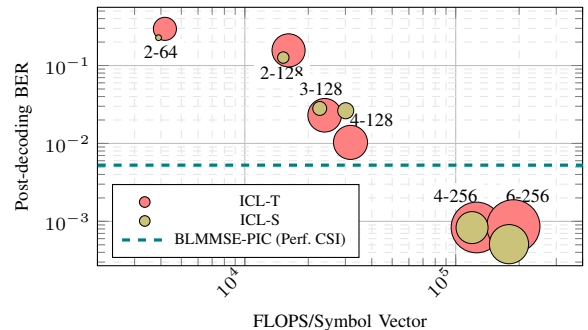


Fig. 12. Post-decoding BER achieved by ICL-T and ICL-S models of varying sizes, compared with the BLMMSE-PIC baseline with perfect CSI. The marker size indicates the model size (in number of parameters), while the data point label (N_L-D_E) indicates the number of layers and embedding dimensions, respectively. Results are evaluated at the 5th turbo iteration under 16-QAM with SNR = 15 dB, $B = 8$, and $T_P = 16$.

token is processed with fixed-length state updates, requiring no recomputation of the entire context sequence.

Fig. 12 shows the post-decoding BER versus the number of FLOPs per symbol vector for each model, where the data label (N_L-D_E) indicates the number of layers and the embedding dimension, respectively. The results confirm that both ICL-T and ICL-S consistently outperform the BLMMSE-PIC baseline, even when the latter is provided with perfect CSI, as long as sufficient model capacity is allocated (e.g., configurations such as $N_L-D_E = 4-256$ and $6-256$). In different configurations, ICL-S generally achieves comparable BER performance as ICL-T, while requiring 50% or fewer parameters and slightly lower computational cost. These findings highlight the strong potential of SSMs as efficient and scalable backbones for resource-constrained wireless applications.

VII. CONCLUSION

This paper introduced a novel ICL framework for soft channel equalization, enabling turbo-compatible, CSI-free, and adaptive detection in coded MIMO systems with quantized receivers. By learning to infer posterior symbol distributions purely from pilot and decoder feedback examples, the proposed ICL-based soft equalizer supports turbo equalization.

Two model variants, based on Transformer and SSMs, were developed and evaluated. Simulations demonstrated that the ICL equalizers consistently outperform conventional model-based baselines, even when the latter are provided with perfect CSI. Particularly, the ICL models showed superior robustness when traditional linear assumptions break down, i.e., under low-resolution quantization and high-order modulations. Moreover, the ICL-based soft equalizers effectively incorporate decoder priors through prompt augmentation, achieving significant performance gains across turbo iterations.

Additionally, we analyzed the generalization ability, model scalability, and computational efficiency of the proposed framework. Results highlight the advantage of Transformer-based models under limited training diversity and the efficiency of SSMs in resource-constrained scenarios.

Overall, this work establishes a new path toward practical neural receivers that are CSI-free, probabilistic, and iterative,

laying the foundation for future adaptable and efficient communication systems leveraging ICL.

REFERENCES

- [1] R. Koetter, A. C. Singer, and M. Tüchler, "Turbo equalization," *IEEE signal processing magazine*, vol. 21, no. 1, pp. 67–80, 2004.
- [2] C. Douillard, M. Jézéquel, C. Berrou, D. Electronique, A. Picart, P. Didier, and A. Glavieux, "Iterative correction of intersymbol interference: turbo-equalization," *European transactions on telecommunications*, vol. 6, no. 5, pp. 507–511, 1995.
- [3] M. Tüchler, A. C. Singer, and R. Koetter, "Minimum mean squared error equalization using a priori information," *IEEE Transactions on Signal Processing*, vol. 50, no. 3, pp. 673–683, 2002.
- [4] C. Studer, S. Fateh, and D. Seethaler, "ASIC implementation of soft-input soft-output MIMO detection using MMSE parallel interference cancellation," *IEEE Journal of Solid-State Circuits*, vol. 46, no. 7, pp. 1754–1765, 2011.
- [5] B. M. Hochwald and S. Ten Brink, "Achieving near-capacity on a multiple-antenna channel," *IEEE transactions on communications*, vol. 51, no. 3, pp. 389–399, 2003.
- [6] C. Studer, M. Wenk, A. Burg, and H. Bolcskei, "Soft-output sphere decoding: Performance and implementation aspects," in *2006 Fortieth Asilomar Conference on Signals, Systems and Computers*. IEEE, 2006, pp. 2071–2076.
- [7] M. Tüchler and A. C. Singer, "Turbo equalization: An overview," *IEEE Transactions on Information Theory*, vol. 57, no. 2, pp. 920–952, 2011.
- [8] A. Lozano and S. Rangan, "Spectral vs energy efficiency in 6G: Impact of the receiver front-end," *arXiv preprint arXiv:2310.02622*, 2023.
- [9] T. Koike-Akino, Y. Wang, D. S. Millar, K. Kojima, and K. Parsons, "Neural turbo equalization: Deep learning for fiber-optic nonlinearity compensation," *Journal of Lightwave Technology*, vol. 38, no. 11, pp. 3059–3066, 2020.
- [10] O. Simeone, S. Park, and J. Kang, "From learning to meta-learning: Reduced training overhead and complexity for communication systems," in *2020 2nd 6G Wireless Summit (6G SUMMIT)*. IEEE, 2020, pp. 1–5.
- [11] M. Zecchin, K. Yu, and O. Simeone, "In-context learning for MIMO equalization using transformer-based sequence models," in *2024 IEEE International Conference on Communications Workshops (ICC Workshops)*, 2024, pp. 1573–1578.
- [12] V. Rajagopalan, V. T. Kunde, C. S. K. Valmeekam, K. Narayanan, S. Shakkottai, D. Kalathil, and J.-F. Chamberland, "Transformers are efficient in-context estimators for wireless communication," *arXiv preprint arXiv:2311.00226*, 2023.
- [13] M. Zecchin, K. Yu, and O. Simeone, "Cell-free multi-user MIMO equalization via in-context learning," in *2024 IEEE 25th International Workshop on Signal Processing Advances in Wireless Communications (SPAWC)*, 2024, pp. 646–650.
- [14] Z. Song, Y. Ma, C. You, H. Yuan, J. Peng, and Y. Gao, "Transformer-based adaptive OFDM MIMO equalization in intelligence-native RAN," in *2024 IEEE/CIC International Conference on Communications in China (ICCC Workshops)*. IEEE, 2024, pp. 179–184.
- [15] L. Fan, J. Yang, and C. Shen, "Decision feedback in-context symbol detection over block-fading channels," *arXiv preprint arXiv:2411.07600*, 2024.
- [16] E. P. da Silva and M. P. Yankov, "Adaptive turbo equalization for nonlinearity compensation in wdm systems," *Journal of Lightwave Technology*, vol. 39, no. 22, pp. 7124–7134, 2021.
- [17] J. Liu, Z. Luo, and X. Xiong, "Low-resolution ADCs for wireless communication: A comprehensive survey," *IEEE Access*, vol. 7, pp. 91 291–91 324, 2019.
- [18] A. Mezghani and J. A. Nossek, "Analysis of Rayleigh-fading channels with 1-bit quantized output," in *2008 IEEE International Symposium on Information Theory*. IEEE, 2008, pp. 260–264.
- [19] Y. Li, C. Tao, G. Seco-Granados, A. Mezghani, A. L. Swindlehurst, and L. Liu, "Channel estimation and performance analysis of one-bit massive MIMO systems," *IEEE Transactions on Signal Processing*, vol. 65, no. 15, pp. 4075–4089, 2017.
- [20] T. Raviv, S. Park, O. Simeone, and N. Shlezinger, "Modular model-based Bayesian learning for uncertainty-aware and reliable deep MIMO receivers," in *2023 IEEE International Conference on Communications Workshops (ICC Workshops)*, 2023, pp. 1032–1037.
- [21] T. Raviv, S. Park, O. Simeone, Y. C. Eldar, and N. Shlezinger, "Adaptive and flexible model-based AI for deep receivers in dynamic channels," *IEEE Wireless Communications*, 2024.
- [22] T. Raviv and N. Shlezinger, "Modular hypernetworks for scalable and adaptive deep MIMO receivers," *arXiv preprint arXiv:2408.11920*, 2024.
- [23] Z. Song, O. Simeone, and B. Rajendran, "Neuromorphic in-context learning for energy-efficient MIMO symbol detection," in *2024 IEEE 25th International Workshop on Signal Processing Advances in Wireless Communications (SPAWC)*, 2024, pp. 1–5.
- [24] Z. Song, M. Zecchin, B. Rajendran, and O. Simeone, "In-context learned equalization in cell-free massive MIMO via state-space models," in *2025 IEEE International Conference on Machine Learning for Communication and Networking (ICMLCN)*, 2025.
- [25] R. W. Heath Jr and A. Lozano, *Foundations of MIMO communication*. Cambridge University Press, 2018.
- [26] D. Tse and P. Viswanath, *Fundamentals of wireless communication*. Cambridge university press, 2005.
- [27] M. Sellathurai and S. Haykin, "Turbo-BLAST for wireless communications: Theory and experiments," *IEEE Transactions on Signal Processing*, vol. 50, no. 10, pp. 2538–2546, 2002.
- [28] F.-S. Shiao, D. P. Taylor, and P. A. Martin, "Combined channel estimation and turbo equalization on wireless channels," in *2008 IEEE 68th Vehicular Technology Conference*. IEEE, 2008, pp. 1–5.
- [29] Y. L. de Jong and T. J. Willink, "Iterative tree search detection for MIMO wireless systems," *IEEE Transactions on Communications*, vol. 53, no. 6, pp. 930–935, 2005.
- [30] M. Latva-aho and J. Lilleberg, "Parallel interference cancellation in multiuser detection," in *Proceedings of ISSSTA'95 International Symposium on Spread Spectrum Techniques and Applications*, vol. 3, 1996, pp. 1151–1155 vol.3.
- [31] D. Guo, L. Rasmussen, and T. J. Lim, "Linear parallel interference cancellation in long-code CDMA multiuser detection," *IEEE Journal on Selected Areas in Communications*, vol. 17, no. 12, pp. 2074–2081, 1999.
- [32] Z. Luo, M. Zhao, S. Liu, and Y. Liu, "Generalized parallel interference cancellation with near-optimal detection performance," *IEEE Transactions On Signal Processing*, vol. 56, no. 1, pp. 304–312, 2007.
- [33] Y. Zhang, Y. V. Zakharov, and J. Li, "Soft-decision-driven sparse channel estimation and turbo equalization for MIMO underwater acoustic communications," *IEEE Access*, vol. 6, pp. 4955–4973, 2018.
- [34] A. Vaswani, N. Shazeer, N. Parmar, J. Uszkoreit, L. Jones, A. N. Gomez, E. Kaiser, and I. Polosukhin, "Attention is all you need," in *Advances in neural information processing systems*, vol. 30, 2017.
- [35] A. Gu, K. Goel, and C. Ré, "Efficiently modeling long sequences with structured state spaces," *arXiv preprint arXiv:2111.00396*, 2021.
- [36] A. Gu and T. Dao, "Mamba: Linear-time sequence modeling with selective state spaces," *arXiv preprint arXiv:2312.00752*, 2023.
- [37] J. Park, J. Park, Z. Xiong, N. Lee, J. Cho, S. Oymak, K. Lee, and D. Papailiopoulos, "Can mamba learn how to learn? a comparative study on in-context learning tasks," *arXiv preprint arXiv:2402.04248*, 2024.
- [38] F. Helm, N. Daheim, and I. Gurevych, "Token weighting for long-range language modeling," *arXiv preprint arXiv:2503.09202*, 2025.
- [39] I. Loshchilov and F. Hutter, "Decoupled weight decay regularization," *arXiv preprint arXiv:1711.05101*, 2017.
- [40] 3GPP, "NR; Multiplexing and channel coding," 3rd Generation Partnership Project (3GPP), Technical Specification TS 38.212, Jan. 2024, Release 18. [Online]. Available: <https://www.3gpp.org/DynaReport/38212.htm>
- [41] W. E. Ryan *et al.*, "An introduction to LDPC codes," *CRC Handbook for Coding and Signal Processing for Recording Systems*, vol. 5, no. 2, pp. 1–23, 2004.
- [42] E. P. da Silva and M. P. Yankov, "Adaptive turbo equalization for nonlinearity compensation in WDM systems," *Journal of Lightwave Technology*, vol. 39, no. 22, pp. 7124–7134, 2021.
- [43] J. J. Bussgang, "Crosscorrelation functions of amplitude-distorted gaussian signals," Research Laboratory of Electronics, Massachusetts Institute of Technology, Cambridge, MA, Tech. Rep. Technical Report 216, 1952.
- [44] A. Radford, J. Wu, R. Child, D. Luan, D. Amodei, I. Sutskever *et al.*, "Language models are unsupervised multitask learners," *OpenAI blog*, vol. 1, no. 8, p. 9, 2019.
- [45] S. Ge, Y. Zhang, L. Liu, M. Zhang, J. Han, and J. Gao, "Model tells you what to discard: Adaptive KV cache compression for LLMs," *arXiv preprint arXiv:2310.01801*, 2023.